minerals

MDPI

Article

Late Paleozoic Tectonic Evolution of the Northern Great Xing'an Range, Northeast China: Constraints from Carboniferous Magmatic Rocks in the Wunuer Area

Liyang Li [1,2], Chuanheng Zhang [1] and Zhiqiang Feng [3,*]

[1] School of Earth and Resources, China University of Geosciences, Beijing 100083, China; 18698263912@163.com (L.L.)
[2] Langfang Comprehensive Survey Center of Natural Resources, China Geology Survey, Langfang 065000, China
[3] Department of Earth Science and Engineering, Taiyuan University of Technology, Taiyuan 030024, China
* Correspondence: fengzhiqiang@tyut.edu.cn

Abstract: Northeast China composes the main part of the Central Asian Orogenic Belt. Traditionally, Northeast China has been considered a collage of several microcontinental blocks. However, the tectonic evolution of these blocks remains uncertain. Igneous rocks can be used to infer the magmatic histories of the blocks and thus help reconstruct their evolution. In this study, we present new zircon U–Pb and whole-rock geochemical data for Carboniferous igneous rocks from the Wunuer area, northern Great Xing'an Range, Northeast China, to constrain the Carboniferous amalgamation of the united Xing'an–Erguna and Songnen–Zhangguangcai Range massifs. On the basis of zircon U–Pb dating results, we identify two main stages of magmatism, i.e., early Carboniferous (332–329 Ma) and late Carboniferous (312–310 Ma). The early Carboniferous igneous rocks include diorites and granodiorites, with the former being classified as calc-alkaline to tholeiitic and the latter as tholeiitic. Both rock types are enriched in Th and U and depleted in Nb and Ti. The rocks display slightly fractionated rare earth element (REE) patterns, with an enrichment in light REEs and a depletion in heavy (H)REEs. The geochemical characteristics of the early Carboniferous rocks indicate that they formed in a subduction-related continental-arc setting. The late Carboniferous igneous rocks include monzogranites and syenogranites, both of which are classified as high-K calc-alkaline rocks and show enrichment in Th, U, and Rb and depletion in Nb and Ti. The rocks display strongly fractionated REE patterns, with an enrichment in light REEs and a depletion in HREEs. The geochemical characteristics of the late Carboniferous rocks indicate that they formed in a syn-collisional tectonic setting. Combining the new geochronological and geochemical results and inferred tectonic settings with regional magmatic data, we propose a new three-stage model to interpret the late Paleozoic tectonic evolution of the united Xing'an–Erguna and Songnen–Zhangguangcai Range massifs of Northeast China: (1) early Carboniferous (360–340 Ma) subduction of the Paleo-Asian oceanic plate beneath the united Xing'an–Erguna Massif and formation of the Wunuer oceanic basin in the Yakeshi area; (2) early to late Carboniferous (340–310 Ma) sustained subduction of the Paleo-Asian oceanic plate beneath the united Xing'an–Erguna Massif and initiation of subduction of the Wunuer oceanic basin; and (3) late Carboniferous–early Permian (310–275 Ma) syn-collisional to post-collisional tectonic transition between the united Xing'an–Erguna Massif and the Songnen–Zhangguangcai Range Massif.

Keywords: great Xing'an range; central Asian orogenic belt; Carboniferous; igneous rocks; geochronology; geochemistry; tectonic evolution

Citation: Li, L.; Zhang, C.; Feng, Z. Late Paleozoic Tectonic Evolution of the Northern Great Xing'an Range, Northeast China: Constraints from Carboniferous Magmatic Rocks in the Wunuer Area. *Minerals* **2023**, *13*, 1090. https://doi.org/10.3390/min13081090

Academic Editors: Jean-Michel Lafon and Hossein Azizi

Received: 23 June 2023
Revised: 31 July 2023
Accepted: 11 August 2023
Published: 15 August 2023

1. Introduction

The Central Asian Orogenic Belt (CAOB) is one of the largest Phanerozoic accretionary orogens in the world (Figure 1). This belt is bounded by the Siberian Craton to the north

and the Tarim and North China cratons to the south and extends from the Ural Mountains in the west through Kazakhstan, Tien Shan, the Altai Mountains, and Mongolia to the Pacific Ocean in the east [1–15]. This huge orogenic belt developed as a result of multiple accretionary and collisional events during the closure of the Paleo-Asian Ocean [16–20]. As a prime example of Paleozoic continental crust and modification, the tectonic evolution of the CAOB has been intensely studied [4,17,21–23].

Northeast China is located in the eastern CAOB. Traditionally, Northeast China has been considered a collage of several microcontinental blocks from southeast to northeast; i.e., the Jiamusi, Songnen, Xing'an, and Erguna blocks, which are separated by the Mudanjiang fault, the Hegenshan suture zone, and the Xinlin–Xiguitu suture zone, respectively [6,24–40] (Figure 2). Advances in research methods and the development of high-precision geological dating techniques have allowed the attributes of the Precambrian basement of the Erguna and Jiamusi blocks to be established and the Xing'an and Songnen blocks to be recognized as accretionary terranes that formed via subduction and collision [7,8,41,42].

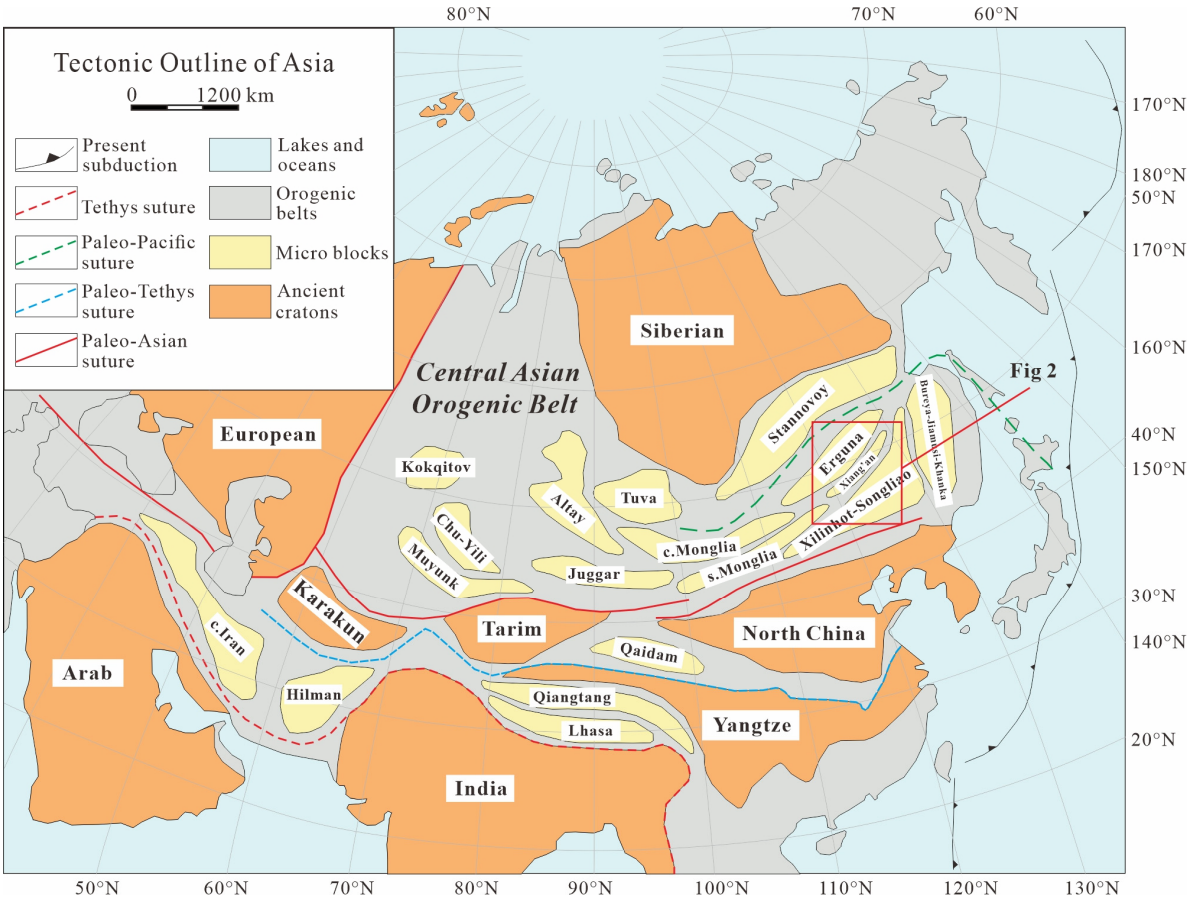

Figure 1. Tectonic sketch map showing the main units of central and eastern Asia (modified after [31,32]).

Uncertainty remains regarding the subduction of paleo-oceanic plates in Northeast China and how and when the amalgamation between the abovementioned blocks/microcontinents took place, especially in regard to the evolution of the Xinlin–Xiguitu suture zone. This suture zone contains the Xinlin ophiolites, Tayuan metagabbros, Jifeng ophiolites, and Yimin blueschists [43–51]. Geochronological data for these units include a K–Ar phlogopite age for the Xinlin ophiolite of 539 Ma [43], a U–Pb zircon age for the Gaxian pyroxenite of 628.4 ± 9.7 Ma [52], a U–Pb zircon age for meta-gabbro from the Huanerku area of 696.8 ± 2.9 Ma [51], a U–Pb zircon age for gabbro from the Jifeng area of 647 ± 5 Ma, and a U–Pb zircon age of greenschist from the Toudaoqiao area of 511 ± 2 Ma.

Early Paleozoic post-orogenic A-type granites reported from the Tahe area are regarded as a product of the closure of the Xinlin–Xiguitu suture zone caused by the collision of the Erguna and Xing'an blocks [24]. The Wunuer ophiolitic mélange occurs in the southwest of the Xinlin–Xiguitu suture zone. This ophiolitic mélange comprises gabbro, diabase, metabasalt, and radiolarian bedded chert with serpentinized amphibole–pyroxene peridotites. Zircon U–Pb dating of the gabbro and diabase has yielded ages of 341 ± 6 and 346 ± 6 Ma, respectively, which suggest that the ophiolite formed during the early Carboniferous. The ophiolite is classified as SSZ type according to geochemical characteristics and may be a late product of a mature back-arc basin tectonic setting [53]. The Xinlin–Xiguitu oceanic basin is generally considered to have closed during the late Cambrian [5–8,24,33,41,50,54]. However, the recent discovery of the early Carboniferous Wunuer ophiolite suggests that the Xinlin–Xiguitu oceanic basin may have closed later than previously thought and that the late Paleozoic tectonic evolution of Northeast China needs to be reassessed.

In this study, we present zircon U–Pb and whole-rock geochemical data for Carboniferous igneous rocks from the Wunuer area, northern Great Xing'an Range, Northeast China, to reconstruct the tectonic evolution of this area during the late Paleozoic, including the opening (by subduction initiation) and closure (by collision) of the Wunuer Ocean. The integration of the new results with previous data allows us to reconstruct the late Paleozoic tectonic evolution of Northeast China.

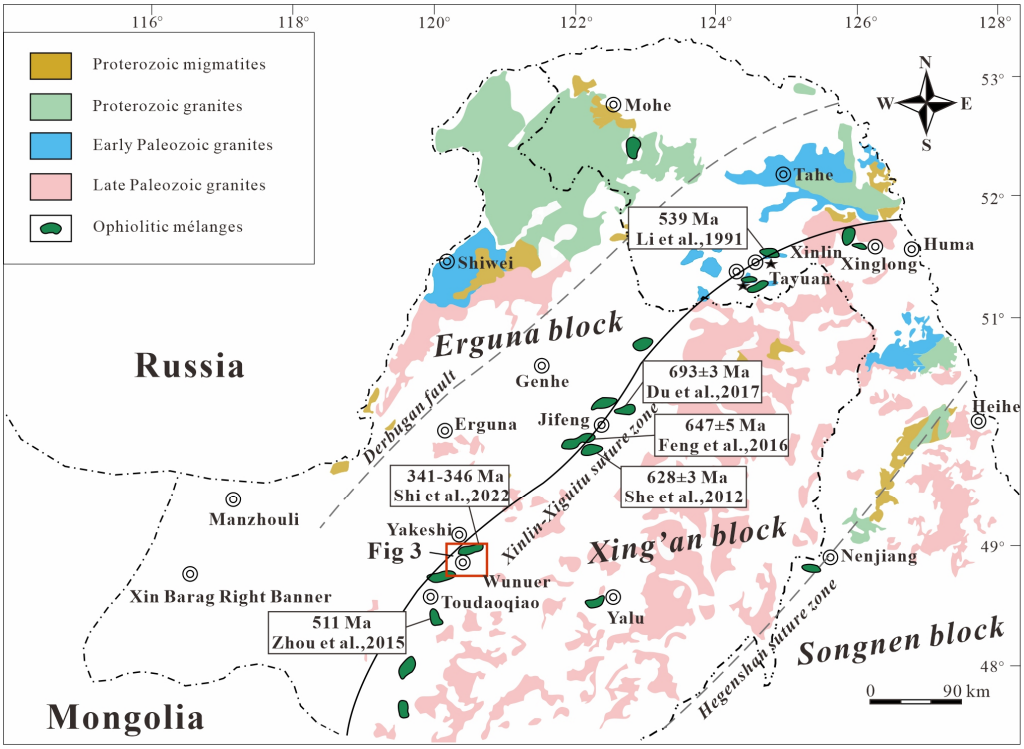

Figure 2. Tectonic division of the central-northern Great Xing'an Range (modified after [50]). Date from [33,43,50–53].

2. Geological Setting and Sample Descriptions

The study area is in the vicinity of Wunuer town, Yakeshi City, in the northern Great Xing'an Range of Inner Mongolia. Tectonically, the study area is located in the Xinlin–Xiguitu suture zone (Figure 2). Ordovician outcrops in the area are composed mainly of the Duobaoshan and Luohe formations. The Duobaoshan Formation comprises a set of intermediate–felsic volcanic rocks with island-arc characteristics [54,55], whereas the Luohe Formation is a set of clastic rocks that formed in an active-continental-margin setting [56,57].

Silurian strata are absent from the study area. Exposed Devonian strata are mainly the Niqiuhe and Daminshan formations, with the former comprising a set of continental-margin clastic rocks [58] and the latter a set of intermediate–felsic volcanic rocks with island-arc characteristics [59]. A large number of late Paleozoic intrusive rocks occur in the study area, including diorite, granodiorite, monzogranite, and syenogranite [60,61], which are emplaced into Ordovician or Devonian strata and overlain by Mesozoic volcanic rocks and Quaternary cover (Figure 3).

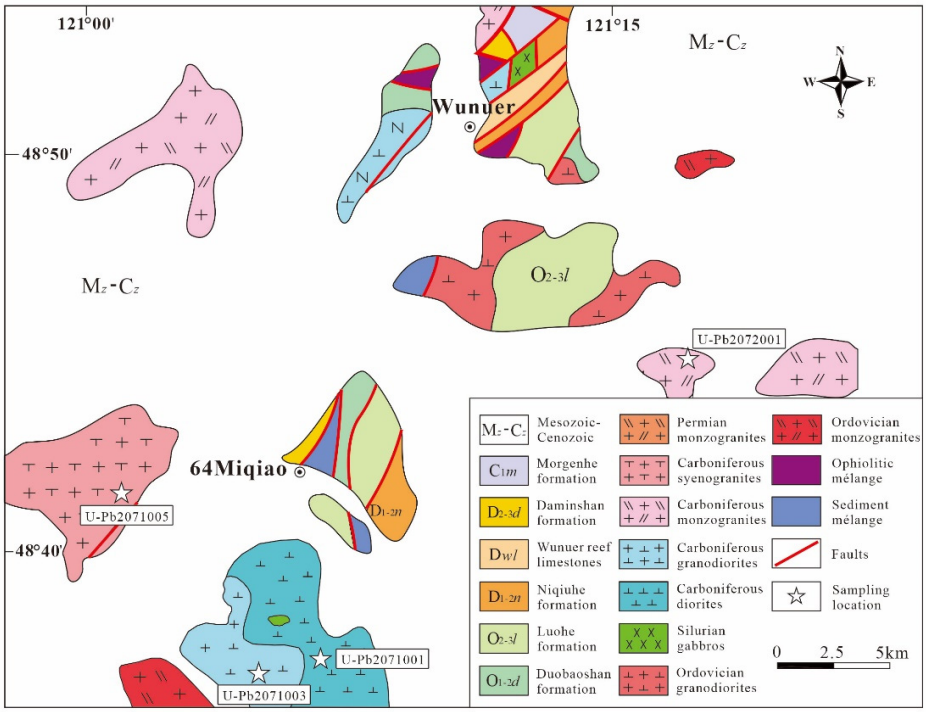

Figure 3. Geological map of Wunuer area with sample locations (simplified and modified after the 1:50,000 geological map).

Intrusive rocks in the Wunuer area include diorite, granodiorite, monzogranite, and syenogranite. A diorite pluton is located ~15 km to the southwest of Wunuer town. The pluton forms an approximately ellipsoidal body with an exposed area of 25 km^2 and intrudes the Devonian Niqiuhe Formation (Figure 3). The diorite is gray to gray-green and has a fine-grained texture (Figure 4a). The rock consists of plagioclase (~55 vol.%), hornblende (~20 vol.%), quartz (~10 vol.%), biotite (~7 vol.%), and K-feldspar (~5 vol.%), with accessory minerals (~3 vol.%) including magnetite, zircon, and apatite.

A granodiorite pluton is located ~16 km to the southwest of Wunuer town. The pluton is an approximately ellipsoidal body with an exposed area of 15 km^2 and intrudes the abovementioned diorite pluton (Figure 3). The granodiorite is light gray to gray-green and has a fine-grained texture (Figure 4b). The rock consists of plagioclase (~45 vol.%), quartz (~20 vol.%), K-feldspar (~15 vol.%), hornblende (~15 vol.%), and biotite (~5 vol.%).

The monzogranite pluton is located ~12 km SE of Wunuer town and is an approximately ellipsoidal body with an exposed area of 20 km^2 (Figure 3). The monzogranite is light pink in color and has a coarse-grained texture (Figure 4c). The rock consists of plagioclase (~40 vol.%), quartz (~25 vol.%), K-feldspar (~30 vol.%), and biotite (~5 vol.%).

The syenogranite pluton is located ~18 km SW of Wunuer town. The pluton is an approximately ellipsoidal body with an exposed area of 32 km^2 (Figure 3). The syenogranite is pink in color and has a coarse-grained texture (Figure 4d). The rock consists of quartz (~25 vol.%), K-feldspar (~60 vol.%), and plagioclase (~15 vol.%).

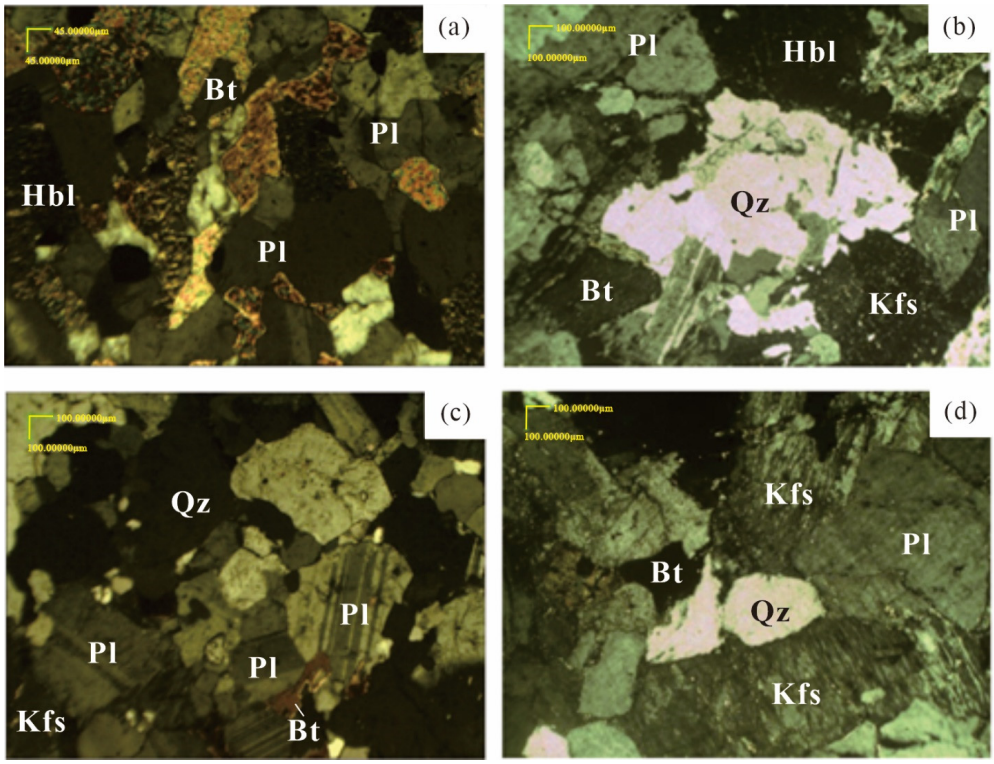

Figure 4. Representative photomicrographs of the Carboniferous intrusive rocks in Wunuer area. (**a**) Diorite (+), (**b**) granodiorite (+), (**c**) monzogranite (+), (**d**) syenogranite (+). Hbl = Hornblende, Bt = biotite, Pl = plagioclase, Kfs = K-feldspar, Qz = quartz.

3. Analytical Methods

One sample for zircon geochronological analysis (U–Pb2071001) and eight samples for geochemical analysis were collected from the diorite pluton. One sample for zircon geochronological analysis (U–Pb2071003) and four samples for geochemical analysis were obtained from the granodiorite pluton. One sample for zircon geochronological analysis (U–Pb2072001) and two samples for geochemical analysis were collected from the monzogranite pluton. One sample for zircon geochronological analysis (U–Pb2071005) and seven samples for geochemical analysis were obtained from the syenogranite pluton.

3.1. Zircon U–Pb Dating

Zircons were separated from samples using conventional heavy liquid and magnetic techniques. Zircon grains were then randomly handpicked in alcohol under a binocular microscope, mounted in epoxy along with zircon standards, and polished to expose grain centers for cathodoluminescence (CL) imaging and U–Pb analysis. CL images were obtained at Beijing Geoanalysis Co., Ltd., Beijing, China. U–Pb analysis was performed by laser-ablation–inductively coupled plasma–mass spectrometry (LA-ICP-MS) at Beijing Createch Testing Technology Co., Ltd., Beijing, China. The analytical instruments used for the dating were a ThermoFisher Neptune multi-receiver ICP-MS instrument and an SIUP193FXArF LA system. The operating conditions during analyses included a laser denudation spot diameter of 35 μm, a laser energy density of 10–13 J/cm^2, and a frequency of 8–10 Hz. Age data were plotted using Isoplot [62].

3.2. Major and Trace Elements

Whole-rock geochemical analyses were performed at the Analytical Laboratory of Beijing Research Institute of Uranium Geology, Beijing, China. Major elements (SiO_2, FeO, TiO_2, Al_2O_3, Fe_2O_3, MgO, MnO, CaO, Na_2O, K_2O, and P_2O_5) were analyzed using an AxiosmAX X-ray fluorescence spectrometer, with an analytical precision of approximately

±5%. Trace elements and rare earth elements (REEs) were analyzed using a NexION300D ICP-MS instrument, with an accuracy better than 10%.

4. Results

4.1. Zircon U–Pb Ages

4.1.1. Early Carboniferous Intrusive Rocks

Most zircon grains from the sampled diorite are subhedral, display oscillatory zoning in CL images (Figure 5a), and have Th/U ratios of 0.62–1.40, indicating a magmatic origin. Analyses of zircons from sample U–Pb2071001 yielded 206Pb/238U ages of 347–310 Ma, with a weighted mean age of 329.7 ± 5.0 Ma (MSWD = 2.3, N = 18; Table S1 and Figure 6a), which is interpreted as the crystallization age of the zircons. The emplacement age of the diorite pluton is therefore inferred to be early Carboniferous.

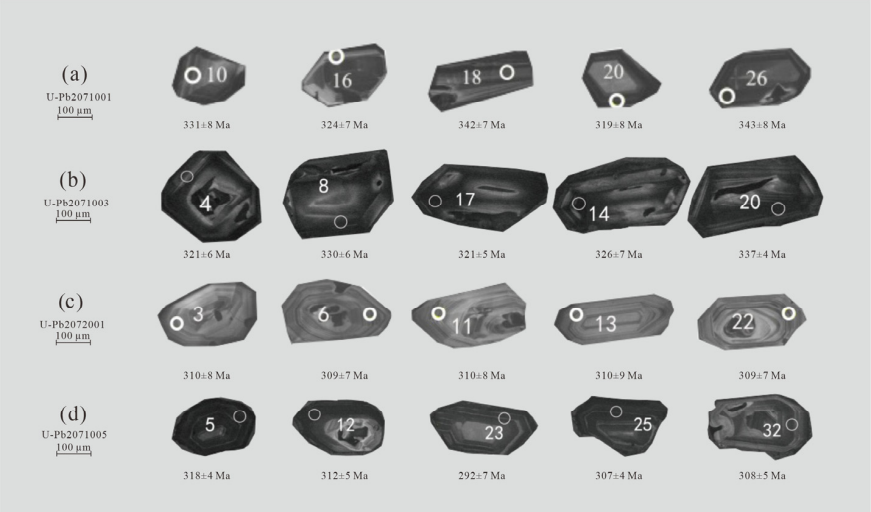

Figure 5. Representative cathodoluminescence (CL) images of zircons from the Carboniferous intrusive rocks in Wunuer area showing their 206Pb/238U ages. (**a**) Diorite, (**b**) granodiorite, (**c**) monzogranite, (**d**) syenogranite.

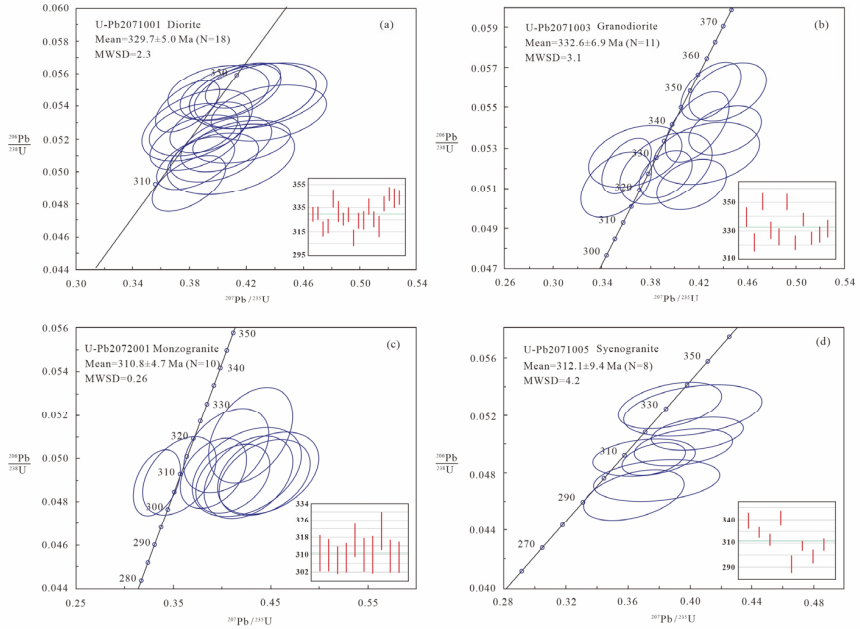

Figure 6. Zircon LA-ICP-MS U-Pb concordant diagrams for zircons from the Carboniferous intrusive rocks in Wunuer area. (**a**) Diorite, (**b**) granodiorite, (**c**) monzogranite, (**d**) syenogranite.

Zircons from the sampled granodiorite are predominantly dark and subhedral, and some display oscillatory zoning in CL images (Figure 5b). The Th/U ratios of the zircons range from 1.04 to 2.68, consistent with a magmatic origin. Analyses of zircons from sample U–Pb2071003 yielded 206Pb/238U ages of 350–322 Ma, with a weighted mean age of 332.6 ± 6.9 Ma (MSWD = 3.1, N = 11; Table S1 and Figure 6b), which is interpreted as the crystallization age of the zircons. The emplacement age of the granodiorite pluton is therefore inferred to be early Carboniferous.

4.1.2. Late Carboniferous Intrusive Rocks

Most zircon grains from the sampled monzogranite are subhedral and display oscillatory zoning in CL images (Figure 5c) with Th/U ratios of 0.63–1.24, indicating a magmatic origin. Analyses of zircons from sample U–Pb2072001 yielded 206Pb/238U ages of 321–308 Ma, with a weighted mean age of 310.8 ± 4.7 Ma (MSWD = 0.26, N = 10; Table S1 and Figure 6c), which is interpreted as the crystallization age of the zircons. The emplacement age of the monzogranite pluton is therefore inferred to be late Carboniferous.

Zircons from the sampled syenogranite are predominantly subhedral, display oscillatory zoning in CL images (Figure 5d), and have Th/U ratios of 0.63–1.19, indicating a magmatic origin. Analyses of zircons from sample U–Pb2071005 yielded 206Pb/238U ages of 331–293 Ma, with a weighted mean age of 312.1 ± 9.4 Ma (MSWD = 4.2, N = 8; Table S1 and Figure 6d), which is interpreted as the crystallization age of the zircons. The emplacement age of the syenogranite pluton is therefore inferred to be late Carboniferous.

4.2. Geochemistry

4.2.1. Major Element Compositions

The sampled diorites have low SiO_2 contents (52.59–57.85 wt.%) and contain Al_2O_3 (15.87–17.11 wt.%), Na_2O + K_2O (3.492–5.31 wt.%), TiO_2 (0.556–1.02 wt.%), Fe_2O_3T (7.54–9.73 wt.%), MgO (0.125–0.18 wt.%), CaO (5.82–8.68 wt.%), and MnO (3.54–5.96 wt.%) (Table 1). These samples are classified mainly as gabbro diorites in a total-alkali–silica (TAS) diagram (Figure 7a), are metaluminous with A/CNK values of 0.75–0.95 (Table 1 and Figure 7b), and are classified as calc-alkaline to tholeiitic in a K_2O vs. SiO_2 diagram (Figure 7c).

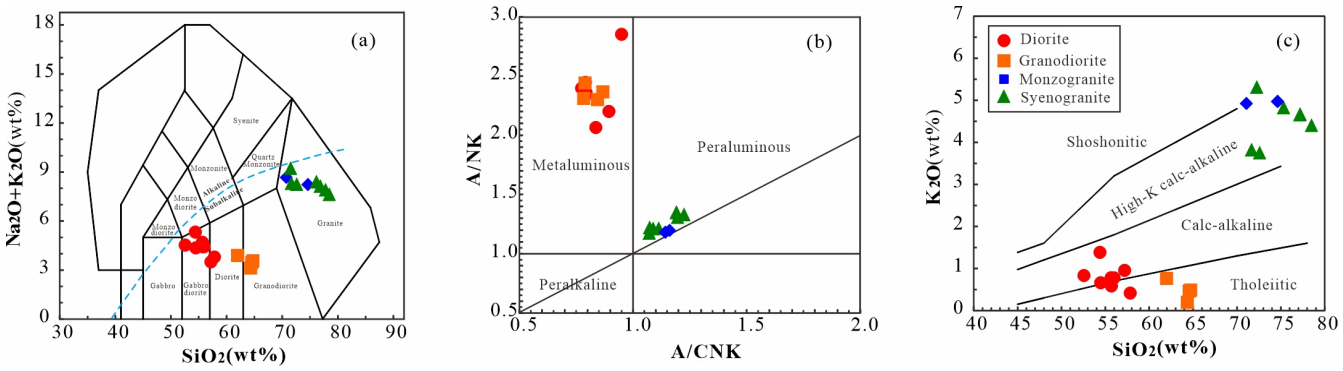

Figure 7. (**a**) SiO_2 versus (Na_2O+K_2O) (after [63]), (**b**) A/CNK(Al_2O_3/(CaO+Na_2O+K_2O)) versus A/NK(Al_2O_3/(Na_2O+K_2O)) diagram (after [64]) and (**c**) SiO_2 versus K_2O diagrams (after [65]).

The sampled granodiorites have low SiO_2 contents (62–64.74 wt.%) and contain Al_2O_3 (12.23–13.77 wt.%), Na_2O + K_2O (3.11–3.88 wt.%), TiO_2 (0.30–0.31 wt.%), Fe_2O_3T (5.93–6.59 wt.%), MgO (0.10–0.12 wt.%), CaO (5.13–6.37 wt.%), and MnO (4.65–5.31 wt.%) (Table 1). These samples are classified mostly as granodiorites in a TAS diagram (Figure 7a), are metaluminous with A/CNK values of 0.78–0.87 (Table 1 and Figure 7b), and are classified as tholeiitic in a K_2O vs. SiO_2 diagram (Figure 7c).

Table 1. Major and trace elements of the Carboniferous intrusive rocks in Wunuer area.

Rocks	**Diorite**									**Granodiorite**			**Monzogranite**			**Syenogranite**				
Sample	**001**	**002**	**003**	**004**	**005**	**006**	**007**	**008**	**009**	**010**	**011**	**012**	**013**	**014**	**015**	**016**	**017**	**018**	**019**	**020**	**021**
Major oxides (wt%)																					
SiO_2	56.01	54.41	57.85	55.68	52.59	54.49	55.71	57.22	62.00	64.74	64.57	64.35	71.07	74.64	76.97	75.10	78.50	72.60	71.68	72.15	76.97
TiO_2	0.78	0.94	0.77	0.90	0.88	1.02	0.82	0.56	0.31	0.30	0.30	0.31	0.38	0.28	0.16	0.21	0.18	0.24	0.24	0.22	0.17
Al_2O_3	16.35	16.43	17.11	16.00	16.28	16.58	16.41	15.87	13.77	12.86	12.81	12.23	14.21	13.30	12.41	13.33	11.65	14.68	15.28	15.57	12.51
TFe_2O_3	7.76	9.12	8.23	8.88	9.57	9.73	8.63	7.54	6.53	5.93	6.19	6.59	3.17	1.56	0.82	0.91	0.70	1.48	1.43	0.98	0.72
MgO	0.18	0.16	0.13	0.15	0.16	0.14	0.15	0.13	0.12	0.11	0.10	0.12	0.04	0.04	0.05	0.04	0.02	0.04	0.03	0.02	0.04
MnO	5.13	5.12	3.54	4.69	5.96	4.39	4.44	4.26	5.18	4.65	5.02	5.31	0.62	0.32	0.14	0.25	0.18	0.53	0.53	0.37	0.15
CaO	7.84	6.40	6.58	5.82	7.44	7.78	7.53	8.68	6.37	5.29	5.13	5.75	0.33	0.26	0.43	0.65	0.42	1.00	1.39	1.09	0.42
Na_2O	3.64	3.93	3.38	3.91	3.69	3.69	3.84	2.54	3.12	3.08	2.99	2.92	3.95	3.39	3.63	3.91	3.22	4.42	4.48	3.86	3.52
K_2O	0.77	1.38	0.41	0.78	0.83	0.66	0.58	0.95	0.76	0.48	0.46	0.19	4.95	4.97	4.67	4.83	4.40	3.75	3.82	5.32	4.66
P_2O_5	0.14	0.13	0.14	0.15	0.13	0.11	0.15	0.07	0.06	0.06	0.06	0.06	0.07	0.04	0.02	0.04	0.03	0.11	0.10	0.08	0.03
LOI	1.38	1.94	1.83	2.99	2.42	1.38	1.71	2.14	1.76	2.40	2.30	2.15	1.20	1.11	0.61	0.64	0.61	1.07	1.01	0.23	0.73
Total	99.48	99.44	99.54	99.45	99.35	99.48	99.56	99.56	99.52	99.43	99.46	99.47	99.90	99.85	99.91	99.91	99.91	99.92	99.99	99.90	99.91
A/NK	2.40	2.06	2.85	2.20	2.34	2.45	2.36	3.05	2.31	2.30	2.36	2.44	1.20	1.21	1.12	1.14	1.16	1.30	1.33	1.28	1.15
A/CNK	0.78	0.84	0.95	0.90	0.79	0.79	0.80	0.76	0.79	0.85	0.87	0.79	1.14	1.16	1.05	1.04	1.08	1.12	1.09	1.11	1.08
Trace elements (ppm)																					
Rb	11.10	27.40	6.78	12.10	18.40	8.73	7.36	13.40	15.50	9.82	6.66	2.66	285.00	320.00	184.00	193.00	164.00	117.00	118.00	155.00	189.00
Ba	144.00	192.00	158.00	200.00	113.00	115.00	107.00	145.00	177.00	147.00	157.00	82.60	546.00	346.00	179.00	179.00	141.00	428.00	553.00	870.00	164.00
Th	1.88	1.49	0.94	1.73	1.87	1.43	1.21	2.57	2.50	3.37	3.00	3.61	19.60	29.80	18.40	19.80	16.70	9.40	11.60	7.90	18.60
U	0.37	0.42	0.38	0.30	0.49	0.49	0.30	0.50	0.42	0.78	0.66	0.89	2.49	2.68	2.37	2.11	1.72	0.10	1.07	0.62	2.04
Ta	0.33	0.26	0.15	0.22	0.21	0.45	0.35	0.23	0.15	0.18	0.16	0.19	1.26	1.40	1.09	1.16	0.10	1.30	1.28	0.97	1.23
Nb	4.18	3.08	2.03	2.50	2.54	6.15	5.08	2.51	2.10	2.32	2.05	2.49	11.50	12.90	11.70	12.60	11.10	7.83	7.39	5.23	13.60
La	13.30	9.06	7.75	8.71	8.94	10.50	10.60	9.37	9.27	9.85	8.49	10.40	31.20	22.90	29.20	35.90	29.70	18.10	22.60	14.40	39.40

Table 1. *Cont.*

Rocks	**Diorite**									**Granodiorite**			**Monzogranite**			**Syenogranite**				
Sample	**001**	**002**	**003**	**004**	**005**	**006**	**007**	**008**	**009**	**010**	**011**	**012**	**013**	**014**	**015**	**016**	**017**	**018**	**019**	**020**	**021**
Ce	33.70	21.70	20.00	19.30	22.30	29.60	31.20	22.30	20.60	20.80	18.60	22.30	86.00	60.30	55.50	65.40	56.20	39.10	47.30	29.40	70.60
Sr	307.00	351.00	351.00	288.00	290.00	310.00	327.00	314.00	273.00	144.00	170.00	214.00	130.00	90.80	45.50	47.90	41.80	449.00	468.00	460.00	44.50
Nd	18.90	14.30	13.90	12.20	14.80	21.10	25.00	13.80	9.71	9.40	8.63	10.70	23.70	16.60	17.20	20.40	17.20	16.40	19.30	12.00	21.70
Zr	48.30	47.50	17.30	31.90	36.10	16.80	14.40	20.70	25.70	46.10	36.10	65.90	55.20	69.10	31.20	36.90	30.60	20.80	22.00	17.50	34.90
Hf	2.13	2.07	1.01	1.71	1.78	1.07	0.85	1.28	1.33	1.88	1.61	2.28	2.63	3.10	2.10	2.38	2.04	0.99	1.12	0.86	2.42
Sm	4.37	3.78	3.83	3.12	3.68	5.22	6.65	3.23	2.12	2.02	1.83	2.27	3.53	3.08	2.90	3.42	2.90	3.14	3.51	2.13	3.66
Y	26.80	24.90	26.40	19.80	20.50	38.20	45.10	18.90	15.50	14.40	13.40	16.30	7.34	11.20	15.60	17.00	13.70	9.09	8.83	5.86	16.90
Yb	2.63	2.42	2.66	2.07	2.02	3.66	4.47	1.99	1.76	1.65	1.56	1.88	0.78	1.17	1.72	1.75	1.32	0.70	0.70	0.48	1.79
Lu	0.41	0.37	0.41	0.31	0.30	0.59	0.69	0.31	0.28	0.26	0.24	0.31	0.19	0.18	0.28	0.27	0.22	0.10	0.10	0.07	0.29
La	13.30	9.06	7.75	8.71	8.94	10.50	10.60	9.37	8.49	9.27	9.85	10.40	31.2	22.90	29.20	35.90	29.70	18.10	22.60	14.40	39.40
Ce	33.70	21.70	20.00	19.30	22.30	29.60	31.20	22.30	18.60	20.60	20.80	22.30	86.00	60.30	55.50	65.40	56.20	39.10	47.30	29.40	70.60
Pr	4.29	2.97	2.79	2.62	3.12	4.50	5.06	3.06	2.15	2.37	2.35	2.60	6.76	4.71	5.20	6.14	5.30	4.26	5.24	3.21	6.56
Nd	18.90	14.30	13.90	12.20	14.80	21.10	25.00	13.80	8.63	9.71	9.40	10.70	23.70	16.60	17.20	20.40	17.20	16.40	19.30	12.00	21.70
Sm	4.37	3.78	3.83	3.12	3.68	5.22	6.65	3.23	1.83	2.12	2.02	2.27	3.53	3.08	2.90	3.42	2.90	3.14	3.51	2.13	3.66
Eu	1.47	1.25	1.24	1.10	1.20	1.51	1.97	1.00	0.41	0.51	0.47	0.48	0.43	0.43	0.39	0.43	0.36	0.63	0.75	0.70	0.44
Gd	4.92	4.38	4.41	3.66	4.02	5.67	7.07	3.55	2.13	2.40	2.26	2.56	3.02	2.83	2.92	3.51	2.93	2.71	3.00	1.91	3.78
Tb	0.75	0.70	0.73	0.60	0.62	0.91	1.17	0.55	0.33	0.37	0.35	0.40	0.31	0.38	0.40	0.47	0.38	0.35	0.37	0.23	0.49
Dy	4.42	4.24	4.48	3.51	3.60	5.47	6.99	3.20	2.04	2.33	2.17	2.51	1.39	1.96	2.19	2.51	1.99	1.72	1.65	1.09	2.58
Ho	0.93	0.90	0.97	0.75	0.75	1.17	1.47	0.67	0.46	0.53	0.49	0.55	0.25	0.39	0.46	0.52	0.40	0.30	0.29	0.19	0.53
Er	2.76	2.67	2.84	2.21	2.23	3.56	4.43	2.03	1.48	1.69	1.59	1.80	0.80	1.16	1.51	1.63	1.25	0.81	0.82	0.54	1.68
Tm	0.40	0.37	0.41	0.31	0.31	0.54	0.66	0.29	0.22	0.26	0.24	0.27	0.11	0.17	0.24	0.25	0.18	0.11	0.11	0.07	0.25
Yb	2.63	2.42	2.66	2.07	2.02	3.66	4.47	1.99	1.56	1.76	1.65	1.88	0.78	1.17	1.72	1.75	1.32	0.70	0.70	0.48	1.79
Lu	0.41	0.37	0.41	0.31	0.30	0.59	0.69	0.31	0.24	0.28	0.26	0.31	0.13	0.18	0.28	0.29	0.22	0.10	0.10	0.07	0.29
Y	26.80	24.90	26.40	19.80	20.50	38.20	45.10	18.90	13.40	15.50	14.40	16.30	7.34	11.20	15.60	17.00	13.70	9.09	8.83	5.86	16.90

Table 1. *Cont.*

Rocks	**Diorite**									**Granodiorite**		**Monzogranite**			**Syenogranite**					
Sample	**001**	**002**	**003**	**004**	**005**	**006**	**007**	**008**	**009**	**010**	**011**	**012**	**013**	**014**	**015**	**016**	**017**	**018**	**019**	**020**	**021**
ΣREE	93.25	69.11	66.41	60.47	67.89	94.00	107.43	65.34	53.90	48.58	54.20	59.03	158.41	116.27	120.11	142.62	120.33	88.44	105.737	66.422	153.75
LREE/HREE	4.42	3.31	2.93	3.51	3.90	3.36	2.99	4.19	4.98	4.74	4.64	4.74	22.34	13.09	11.36	12.05	12.88	12.00	14.03	13.51	12.50
δEu	0.97	0.94	0.92	0.99	0.95	0.84	0.87	0.90	0.66	0.63	0.69	0.61	0.39	0.44	0.41	0.38	0.37	0.65	0.69	1.04	0.36
δCe	1.09	1.02	1.05	0.98	1.03	1.06	1.04	1.02	1.03	1.04	1.05	1.02	1.39	1.35	1.02	0.99	1.01	1.05	1.03	1.02	0.98
LaN/YbN	3.63	2.69	2.09	3.02	3.17	2.06	1.70	3.38	4.28	3.90	3.78	3.97	28.77	14.04	12.18	14.72	16.15	18.60	23.22	21.61	15.80
LaN/SmN	2.18	1.72	1.45	2.00	1.74	1.44	1.14	2.08	3.33	3.14	3.50	3.29	6.34	5.34	7.23	7.53	7.35	4.14	4.62	4.85	7.73
GdN/YbN	1.55	1.50	1.37	1.46	1.65	1.28	1.31	1.48	1.13	1.13	1.13	1.13	3.21	2.00	1.40	1.66	1.84	3.21	3.56	3.31	1.75

The sampled monzogranites have high SiO_2 contents (71.07–74.64 wt.%) and contain Al_2O_3 (13.3–14.21 wt.%), Na_2O + K_2O (8.36–8.9 wt.%), TiO_2 (0.282–0.381 wt.%), Fe_2O_3T (1.36–3.17 wt.%), MgO (0.036–0.044 wt.%), CaO (0.259–0.332 wt.%), and MnO (0.323–0.618 wt.%) (Table 1). These samples are classified as granites in a TAS diagram (Figure 7a), are peraluminous with A/CNK values of 1.14–1.16 (Table 1 and Figure 7b), and are classified as high-K calc-alkaline in a K_2O vs. SiO_2 diagram (Figure 7c).

The sampled syenogranites have high SiO_2 contents (71.68–78.5 wt.%) and contain Al_2O_3 (11.65–15.57 wt.%), Na_2O + K_2O (7.62–9.18 wt.%), TiO_2 (0.16–0.24 wt.%), Fe_2O_3T (0.7–1.48 wt.%), MgO (0.02–0.05 wt.%), CaO (0.42–1.39 wt.%), and MnO (0.14–0.528 wt.%) (Table 1). These samples are classified as granites in a TAS diagram (Figure 7a), are peraluminous with A/CNK values of 1.03–1.12 (Table 1 and Figure 7b), and are classified as high-K calc-alkaline in a K_2O vs. SiO_2 diagram (Figure 7c).

4.2.2. Trace Element Compositions

The sampled diorites are relatively enriched in Th and U and depleted in some high-field-strength elements (HFSEs; e.g., Nb and Ti). The rocks display slightly fractionated REE patterns between light REEs (LREEs) and heavy REEs (HREEs) (LREE/HREE = 2.93–4.42, (La/Yb)N = 1.7–3.63), with LREE enrichment, HREE depletion, and slight or no negative Eu anomalies (Eu/Eu* = 0.84–0.99) (Table 1 and Figure 8a,b).

The sampled granodiorites are relatively enriched in Th and U and depleted in some HFSEs (e.g., Nb and Ti). The rocks display lightly fractionated REE patterns (LREE/HREE = 4.64–4.98, (La/Yb)N = 3.78–4.28), with LREE enrichment, HREE depletion, and negative Eu anomalies (Eu/Eu* = 0.61–0.69) (Table 1 and Figure 8c,d).

The sampled monzogranites are enriched in Th, U, and large-ion lithophile elements (LILEs; e.g., Rb) and depleted in some HFSEs (e.g., Nb and Ti). The rocks display strongly fractionated REE patterns (LREE/HREE = 13.09–22.34, (La/Yb)N = 14.04–28.77), with LREE enrichment, HREE depletion, and negative Eu anomalies (Eu/Eu* = 0.39–0.44) (Table 1 and Figure 8e,f).

The sampled syenogranites are enriched in Th, U, and LILEs (e.g., Rb and K) and depleted in some HFSEs (e.g., Nb and Ti). The rocks display strongly fractionated REE patterns (LREE/HREE = 11.36–14.03, (La/Yb)N = 12.18–23.22), with LREE enrichment, HREE depletion, and negative Eu anomalies (Eu/Eu* = 0.36–1.04) (Table 1 and Figure 8g,h).

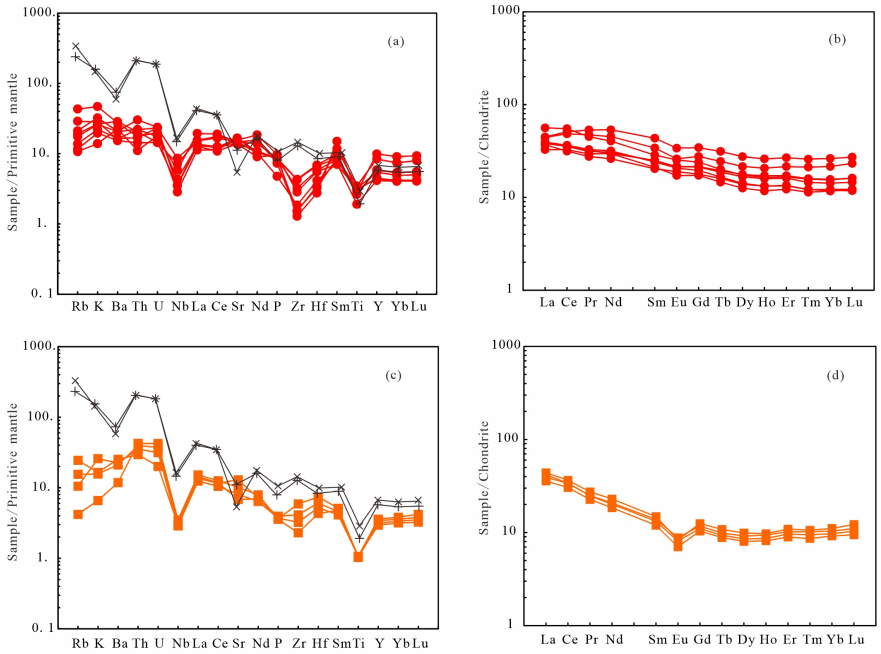

Figure 8. *Cont.*

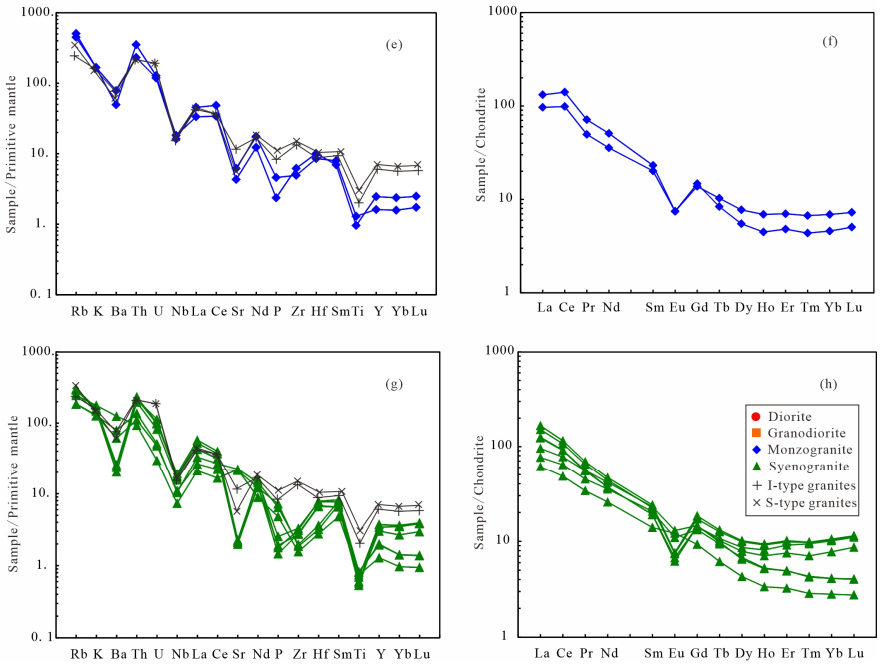

Figure 8. Primitive-mantle-normalized trace element spidergrams (**a**,**c**,**e**,**g**) and Chondrite-normalized REE patterns (**b**,**d**,**f**,**h**).

5. Discussion

5.1. Carboniferous Intrusive Rocks in the Great Xing'an Range

According to our geochronological analyses, the studied diorite and granodiorite were emplaced during the early Carboniferous, and the syenogranite and monzogranite were emplaced during the late Carboniferous. There are widespread occurrences of coeval magmatic rocks in the Great Xing'an Range. Most of the early Carboniferous intrusive rocks are distributed in a strip along the Xinlin–Xiguitu and Hegenshan suture zones (Figure 9). The late Carboniferous intrusive rocks have a wider distribution, occurring mainly in the Yakeshi, Duobaoshan, Zhalantun, Heihe, and Wudalianchi areas.

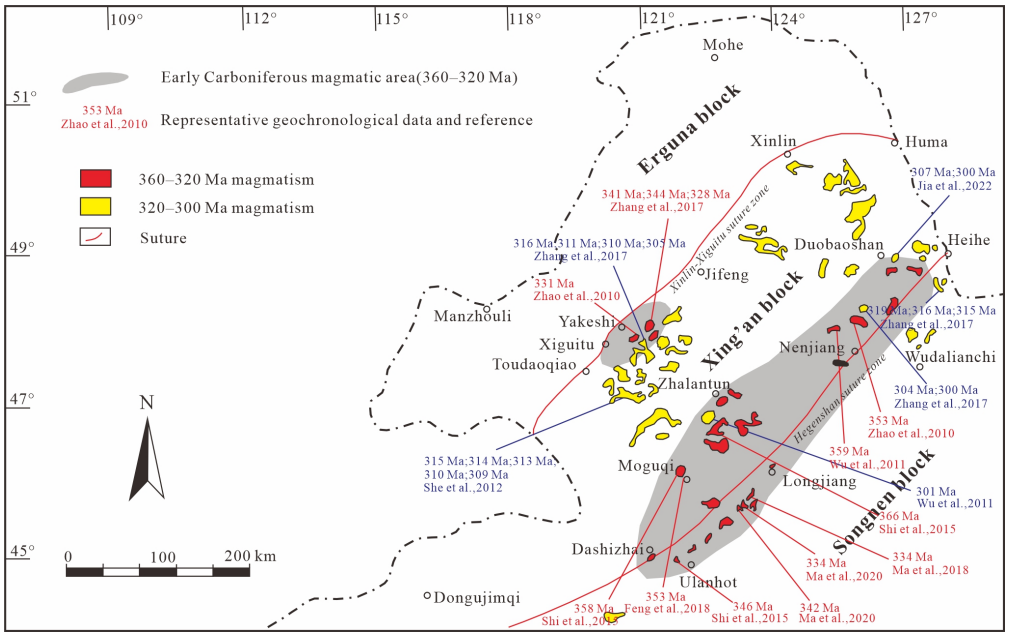

Figure 9. Distribution of the Carboniferous intrusive rocks in northern Great Xing'an Range, Northeast China. Date from [28,52,60,66–73].

5.2. Petrogenesis of Carboniferous Intrusive Rocks in the Northern Great Xing'an Range

5.2.1. Petrogenesis of the Wunuer Early Carboniferous Igneous Rocks

Early Carboniferous igneous rocks in the Wunuer area comprise diorite and granodiorite. These rocks contain hornblende and biotite but no primary muscovite. The mineral assemblages are consistent with those of I-type granites [74–79]. A/CNK values (0.75–0.95) classify the diorites and granodiorites as metaluminous rocks. The rocks are characterized by relatively high Al_2O_3, Fe, Mg, and Sr and low Si and K contents, the enrichment in LILEs and LREEs, and the depletion in HREEs. The granodiorites plot in the I-type and S-type granite fields in the Nb–(10,000 Ga/Al), Ce–(10,000 Ga/Al), and Y–(10,000 Ga/Al) diagrams (Figure 10a–c) and mainly in the I-type granite field in an ACF diagram (Figure 10d).

The average value of Rb/Sr for the diorite and granodiorite is 0.04, which is close to the primitive mantle (0.03), E-MORB (0.033), and OIB (0.047) [80], but lower than the crustal ratio (0.15). These geochemical characteristics suggest that the diorite and granodiorite are sourced from partial malting of the mantle.

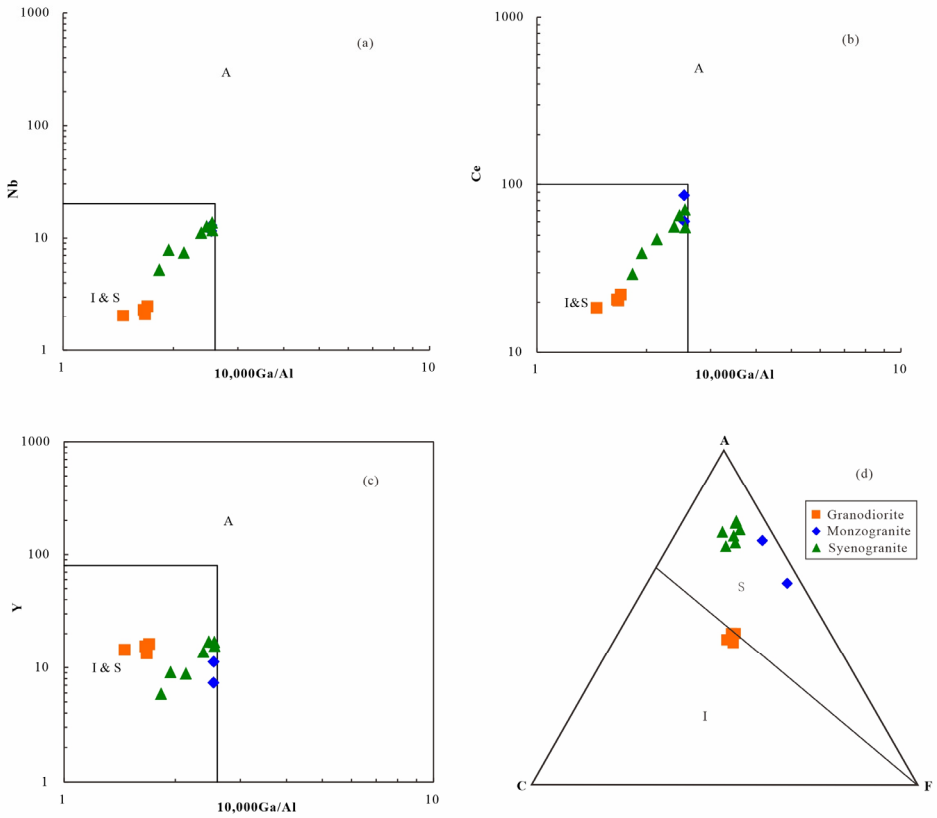

Figure 10. (**a**) Nb versus 10,000 Ga/Al diagram (after [81]), (**b**) Ce versus 10,000 Ga/Al diagram (after [81]), (**c**) Y versus 10,000 Ga/Al diagram (after [81]), (**d**) ACF diagram (after [82]).

5.2.2. Petrogenesis of the Wunuer Late Carboniferous Igneous Rocks

Late Carboniferous igneous rocks in the Wunuer area comprise monzogranite and syenogranite. These rocks are composed predominantly of quartz, K-feldspar, and plagioclase. A/CNK values (1.03–1.16) classify the monzogranites and syenogranites as peraluminous rocks. The rocks are characterized by relatively high SiO_2 and K_2O and low P_2O_5 contents, the enrichment in Rb, Th, and U, and the depletion in Ba, Nb, Ta, Sr, P, and Ti. These characteristics are consistent with those of S-type granites. The monzogranites and syenogranites plot in the I-type and S-type granite fields in Nb—(10,000 Ga/Al), Ce—(10,000 Ga/Al), and Y—(10,000 Ga/Al) diagrams (Figure 10a–c) and mostly in the S-type granite field in an ACF diagram (Figure 10d).

The average value of Rb/Sr for the monzogranite and syenogranite is 2.53, which is close to the crustal ratio (0.15) but higher than the primitive mantle (0.03), E-MORB (0.033), and OIB (0.047) [80]. These geochemical characteristics suggest that the monzogranite and syenogranite are sourced from partial melting of the crust.

5.3. Inferred Tectonic Settings

The geochemical characteristics of the diorites and granodiorites (Section 4.2) are consistent with formation in a subduction-related continental-arc setting, and those of the monzogranites and syenogranites suggest formation in a syn-collisional tectonic setting. The granodiorites plot in the volcanic arc fields in Rb–(Y + Nb) and Rb–(Yb + Ta) diagrams (Figure 11a,b) and mostly in the volcanic arc fields in Rb/10–Hf–3Ta and Rb/30–Hf–3Ta diagrams (Figure 11c,d). The syenogranites and monzogranites fall predominantly in the syn-collisional fields in Rb–(Y + Nb) and Rb–(Yb + Ta) diagrams (Figure 11a,b) and in the syn-collisional fields in Rb/10–Hf–3Ta and Rb/30–Hf–3Ta diagrams (Figure 11c,d).

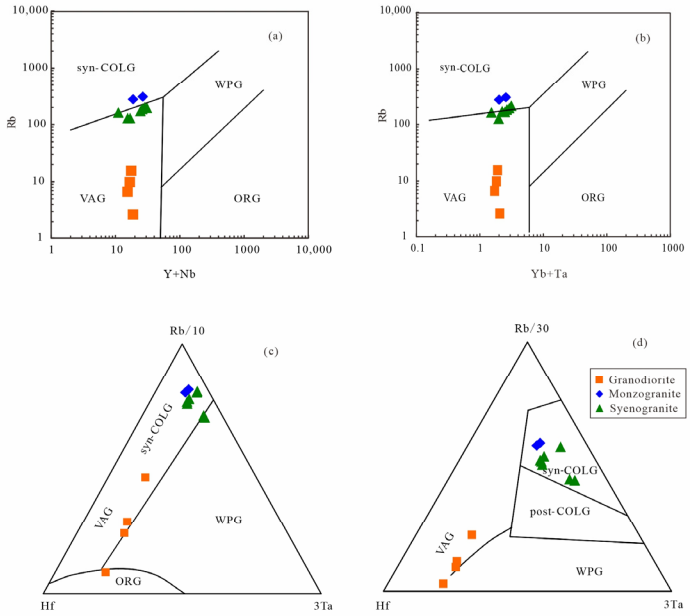

Figure 11. (**a**) Rb versus Y+Nb diagram (after [83]), (**b**) Rb versus Yb+Ta diagram (after [83]), (**c**) Rb/10-Hf-3Ta diagram (after [84]), (**d**) Rb/30-Hf-3Ta diagram (after [84]). VAG = volcanic arc granites, WPG = within plate granites, COLG = collisional granites, and ORG = oceanic ridge granites.

5.4. Tectonic Implications

The integrated results of this study, combined with regional geological data, allow a new model to be proposed for the late Paleozoic tectonic evolution of the northern Great Xing'an Range (Figure 12), as follows. During the early Carboniferous (360–340 Ma), subduction of the Paleo-Asian oceanic plate beneath the united Xing'an–Erguna Massif occurred, with the associated development of a back-arc ocean basin (the Wunuer oceanic basin). The early Carboniferous igneous rocks (360–340 Ma) display markedly different rock associations and geochemical characteristics from east to west across the Xing'an block. Igneous rocks in the east of the Xing'an block (the Heihe, Nenjiang, Zhalantun, and Moguqi areas) are composed of gabbro, gabbro diorite, monzogranite, and syenogranite and are classified as calc-alkaline, consistent with formation in a subduction-related setting [41,85–88]. In contrast, ophiolites and gabbros in the west of the Xing'an block (the Wunuer area) are consistent with a back-arc ocean basin setting, for example, the age of the Wunuer ophiolitic mélange is 341~346 Ma; the Wunuer ophiolitic mélange is classified as SSZ type according to geochemical characteristics and may be a late product of a mature back-arc basin tectonic setting [53]. We suggest that early Carboniferous igneous

rocks formed as a result of northwest-directed subduction of the Paleo-Asian oceanic plate, which was initiated during the late Devonian [66,89]. The continuous subduction of the Paleo-Asian oceanic slab generated a magmatic arc encompassing the Heihe, Nenjiang, Zhalantun, and Mogiqi areas, as well as the Wunuer back-arc oceanic basin in the Wunuer area [53,60,66,90–92].

During the early–late Carboniferous (340–310 Ma), sustained subduction of the Paleo-Asian oceanic plate and subduction of the Wunuer oceanic basin occurred. Igneous rocks in the east of the Xing'an block (the Longzhen and Yaergenchu areas) are composed of granodiorite and monzogranite, which are classified as calc-alkaline series, implying formation in a subduction-related setting [93,94]. The diorite, granodiorite, monzogranite, and syenogranite in the west of the Xing'an block (Tahe, Taerqi, and Wunuer areas) formed in a subduction-related setting, indicating that the Wunuer oceanic basin had entered the subduction phase [28,52,95,96].

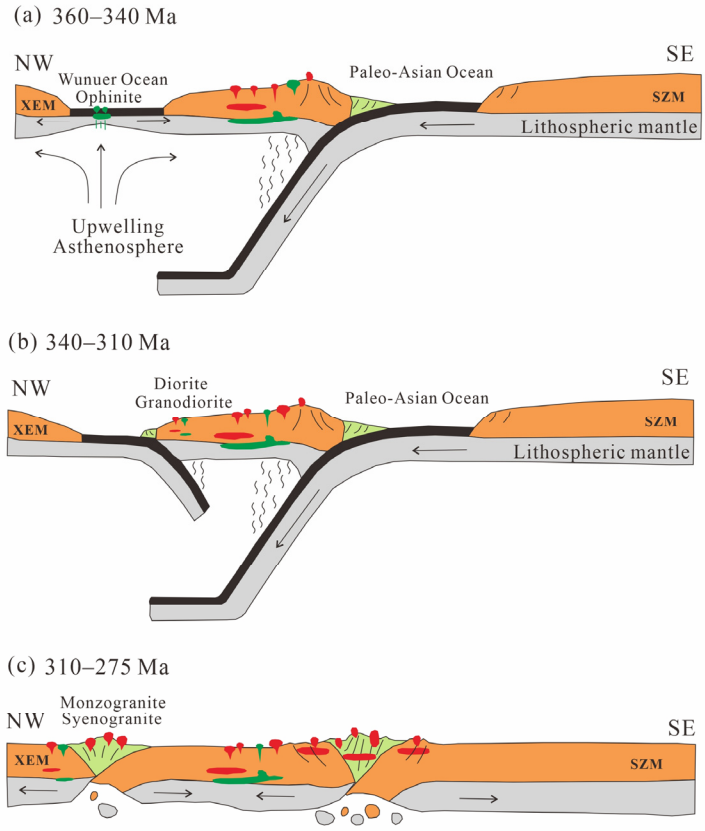

Figure 12. Cartoon diagram showing tectonic evolution during late Devonian to early Permian (ca. 360–275 Ma) of the northern Great Xing'an Range, Northeast China. XEM = the united Xing'an–Erguna Massif; SZM = the Songnen–Zhangguangcai Range Massif.

The late Carboniferous–early Permian (310–275 Ma) was characterized by a syn-collisional to post-collisional tectonic setting between the united Xing'an–Erguna Massif and the Songnen–Zhangguangcai Range Massif. The widely distributed late early Carboniferous–early Permian igneous rocks in the northern Great Xing'an Range are composed mostly of syenogranite and monzogranite and signify a syn-collisional setting [61,67,96]. The occurrence of early Permian alkaline rocks implies a subsequent extensional tectonic environment in a post-collisional setting [52,67]. Therefore, we suggest that the late Carboniferous–early Permian igneous rocks formed in a syn-collisional to post-collisional transitional setting in the Wunuer and Taerqi areas [52,67,96] and in the Heihe, Duobaoshan, Nenjiang, and Zhalantun areas [28,67,68,97], implying that both the Wunuer Ocean and Paleo-Asian Ocean had closed.

6. Conclusions

We generated new zircon U–Pb and whole-rock geochemical data for Carboniferous igneous rocks from the Wunuer area, northern Great Xing'an Range, to reconstruct the late Paleozoic tectonic evolution of this area and, in combination with regional geological and geochronological data, to establish an integrated tectonic history of Northeast China. The main conclusions of this study are as follows:

(1) Intrusive rocks in the Wunuer area include diorite, granodiorite, monzogranite, and syenogranite. The zircon U–Pb mean ages of the diorite and granodiorite are 329.7 ± 5.0 and 332.6 ± 6.9 Ma, respectively, indicating early Carboniferous emplacement of these rocks. The zircon U–Pb mean ages of the monzogranite and syenogranite are 310.8 ± 4.7 and 312.1 ± 9.4 Ma, respectively, indicating late Carboniferous emplacement.

(2) The geochemical signatures of the Wunuer rocks indicate that the diorite and granodiorite formed in a subduction-related continental-arc setting and that the syenogranite and monzogranite formed in a syn-collisional tectonic setting.

(3) A new three-stage model for the late Paleozoic tectonic evolution of Northeast China is proposed: (1) early Carboniferous (360–340 Ma) subduction of the Paleo-Asian oceanic plate beneath the united Xing'an–Erguna Massif and formation of the Wunuer oceanic basin in the Yakeshi area; (2) early Carboniferous–late Carboniferous (340–310 Ma) subduction of the Paleo-Asian oceanic plate beneath the united Xing'an–Erguna Massif and initiation of subduction of the Wunuer oceanic basin; and (3) late Carboniferous–early Permian (310–275 Ma) syn-collisional to post-collisional tectonic transition between the united Xing'an–Erguna and Songnen–Zhangguangcai Range massifs.

Supplementary Materials: The following supporting information can be downloaded froom: https://www.mdpi.com/article/10.3390/min13081090/s1, Table S1: LA-ICP-MS U-Pb-Th data for zircons for the Carboniferous intrusive rocks in Wunuer area.

Author Contributions: Conceptualization, L.L. and Z.F.; methodology, L.L.; software, L.L.; validation, L.L., C.Z. and Z.F.; formal analysis, L.L.; investigation, L.L., C.Z. and Z.F.; resources, L.L. and Z.F.; data curation, L.L.; writing—original draft preparation, L.L.; writing—review and editing, L.L., C.Z. and Z.F.; visualization, L.L.; supervision, L.L., C.Z. and Z.F.; project administration, L.L. and Z.F.; funding acquisition, L.L. All authors have read and agreed to the published version of the manuscript.

Funding: This research was funded by the China Geological Survey Project (DD20230251, DD2016007808) and supported by the National Natural Science Foundation of China (Grant No. 42272251, 42072230 and 41602235) and National Science Foundation for Post-doctoral Scientists of China (Grant No. 2019M661060).

Data Availability Statement: The original contributions presented in the study are included in the article/Supplementary Materials.

Acknowledgments: We thank Yueqiang Qin, and Xin Feng of Langfang Comprehensive Survey Center of Natural Resources for his helpful discussions during research process. Special thanks are due to the reviewers and editors of this journal for their valuable suggestions and revisions of the manuscript.

Conflicts of Interest: The authors declare no conflict of interest.

References

1. Jahn, B.M.; Wu, F.Y.; Chen, B. Granitoids of the Central Asian Orogenic Belt and continental growth in the Phanerozoic. *Trans. R. Soc. Edinb.* **2000**, *91*, 181–194.
2. Jahn, B.M.; Wu, F.Y.; Chen, B. Massive granitoid generation in Central Asia: Nd isotope evidence and implication for continental growth in the Phanerozoic. *Episodes* **2000**, *23*, 82–92. [CrossRef] [PubMed]
3. Kröner, A.; Windley, B.F.; Badarch, G. Accretionary growth and crust-formation in the Central Asian Orogenic Belt and comparison with the Arabian–Nubian shield. *Geol. Soc. Am. Mem.* **2007**, *200*, 181–209.
4. Kröner, A.; Kovach, V.; Belousova, E.; Hegner, E.; Armstrong, R.; Dolgopolova, A.; Seltmann, R.; Alexeiev, D.V.; Hoffmann, J.E.; Wong, J. Reassessment of continental growt during the accretionary history of the Central Asian Orogenic Belt. *Gondwana Res.* **2014**, *25*, 103–125. [CrossRef]

5. Liu, Y.J.; Feng, Z.Q.; Jiang, L.W.; Jin, W.; Li, W.M.; Guan, Q.B.; Wen, Q.B.; Liang, C.Y. Ophiolite in the eastern Central Asian Orogenic Belt, NE China. *Acta Petrol. Sin.* **2019**, *35*, 3017–3047. (In Chinese with English Abstract)
6. Liu, Y.J.; Li, W.M.; Feng, Z.Q.; Wen, Q.B.; Neubauer, F.; Liang, C.Y. A review of the Paleozoic tectonics in the eastern part of Central Asian Orogenic Belt. *Gondwana Res.* **2017**, *43*, 123–148. [CrossRef]
7. Liu, Y.J.; Li, W.M.; Ma, Y.F.; Feng, Z.Q.; Guan, Q.B.; Li, S.Z.; Chen, Z.X.; Liang, C.Y.; Wen, Q.B. An orocline in the eastern Central Asian Orogenic Belt. *Earth-Sci. Rev.* **2021**, *221*, 103808. [CrossRef]
8. Liu, Y.J.; Ma, Y.F.; Feng, Z.Q.; Li, W.M.; Li, S.Z.; Guan, Q.B.; Chen, Z.X.; Zhou, T.; Fang, Q.A. Paleozoic Orocline in the eastern Central Asian Orogenic Belt. *Acta Geol. Sin.* **2022**, *96*, 3468–3493. (In Chinese with English Abstract)
9. Safonova, I.Y.; Kotlyarov, A.; Krivonogov, S.; Xiao, W.J. Intra-oceanic arcs of the PaleoAsian Ocean. *Gondwana Res.* **2011**, *50*, 167–194. [CrossRef]
10. Safonova, I.; Maruyama, S. Asia: A frontier for a future supercontinent Amasia. *Int. Geol. Rev.* **2014**, *56*, 1051–1071. [CrossRef]
11. Yarmolyuk, V.V.; Kovach, V.P.; Kozakov, I.K. Mechanisms of continental crust formation in the Central Asian Foldbelt. *Geotectonics* **2012**, *46*, 251–272. [CrossRef]
12. Xiao, W.J.; Windley, B.F.; Allen, M.B.; Han, C.M. Paleozoic multiple accretionary and collisional tectonics of the Chinese Tianshan orogenic collage. *Gondwana Res.* **2013**, *23*, 1316–1341. [CrossRef]
13. Xiao, W.J.; Santosh, M. The western Central Asian Orogenic Belt: A window to accretionary orogenesis and continental growth. *Gondwana Res.* **2014**, *25*, 1429–1444. [CrossRef]
14. Kovalenko, V.I.; Yarmolyuk, V.V.; Kovach, V.P.; Kotov, A.B.; Kozakov, I.K.; Salnikova, E.B.; Larin, A.M. Isotope provinces, mechanisms of generation and sources of the continental crust in the Central Asian mobile belt: Geological and isotopic evidence. *J. Asian Earth Sci.* **2004**, *23*, 605–627. [CrossRef]
15. Safonova, I.Y.; Santosh, M. Accretionary complexes in the Asia–Pacific region: Tracing archives of ocean plate stratigraphy and tracking mantle plumes. *Gondwana Res.* **2014**, *25*, 126–158. [CrossRef]
16. Dobretsov, N.L.; Berzin, N.A.; Buslov, M.M. Opening and tectonic evolution of the Paleo-Asian Ocean. *Int. Geol. Rev.* **1995**, *37*, 335–360. [CrossRef]
17. Xiao, W.J.; Windley, B.F.; Hao, J.; Zhai, M.G. Accretion leading to collision and the Permian Solonker suture, Inner Mongolia, China: Termination of the central Asian orogenic belt. *Tectonic* **2003**, *22*, 8.1–8.20. [CrossRef]
18. Windley, B.F.; Alexeiev, D.; Xiao, W.J.; Kröner, A.; Badarch, G. Tectonic models for accretion of the Central Asian Orogenic Belt. *J. Geol. Soc.* **2007**, *164*, 31–47. [CrossRef]
19. Safonova, I.Y.; Sennikov, N.V.; Komiya, T. Geochemical diversity in oceanic basalts hosted by the Zasur'ya accretionary complex, NW Russian Altai, Central Asia: Implications from trace elements and Nd isotopes. *J. Asian Earth Sci.* **2011**, *42*, 191–207. [CrossRef]
20. Safonova, I.Y. Juvenile versus recycled crust in the Central Asian Orogenic Belt: Implications from ocean plate stratigraphy, blueschist belts and intraoceanic arcs. *Gondwana Res.* **2017**, *47*, 6–27. [CrossRef]
21. Li, J.Y. Permian geodynamic setting of Northeast China and adjacent regions: Closure of the Paleo-Asian Ocean and subduction of the Paleo-Pacific Plate. *J. Asian Earth Sci.* **2006**, *26*, 207–224. [CrossRef]
22. Kröner, A.; Lehmann, J.; Schulmann, K.; Demoux, A.; Lexa, O.; Tomurhuu, D.; Stipska, P.; Liu, D.; Wingate, M.T.D. Lithostratigraphic and geochronological constraints on the evolution of the Central Asian Orogenic Belt in SW Mongolia: Early Paleozoic rifting followed by late Paleozoic accretion. *Am. J. Sci.* **2010**, *310*, 523–574. [CrossRef]
23. Zheng, Y.F.; Xiao, W.J.; Zhao, G.C. Introduction to tectonic of China. *Gondwana Res.* **2013**, *23*, 1189–1206. [CrossRef]
24. Ge, W.C.; Wu, F.Y.; Zhou, C.Y.; Abdel Rahman, A.A. Emplacement age of the Tahe granite and its constraints on the tectonic nature of the Erguna block in the northern part of the Da Xing'an Range. *Chin. Sci. Bull.* **2005**, *50*, 2097–2105. (In Chinese with English Abstract) [CrossRef]
25. Miao, L.C.; Fan, W.M.; Zhang, F.Q.; Liu, D.Y.; Jian, P.; Shi, G.H.; Tao, H.; Shi, Y.R. Zircon SHRIMP geochronology of the Xinkailing-Kele complex in the northwestern Lesser Xing'an Range, and its geological implications. *Chin. Sci. Bull.* **2004**, *49*, 201–209. (In Chinese with English Abstract) [CrossRef]
26. Miao, L.C.; Liu, D.Y.; Zhang, F.Q. Zircon SHRIMP U-Pb ages of the "Xinghuadukou Group" in Hanjiayuanzi and Xinlin areas and the "Zhalantun Group" in Inner Mongolia, Da Hinggan Mountains. *Chin. Sci. Bull.* **2007**, *52*, 1112–1134. (In Chinese with English Abstract) [CrossRef]
27. Miao, L.C.; Zhang, F.C.; Jiao, S.J. Age, protoliths and tectonic implications of the Toudaoqiao blueschist Inner Mongolia, China. *J. Asian Earth Sci.* **2015**, *105*, 360–373. [CrossRef]
28. Wu, F.Y.; Sun, D.Y.; Ge, W.C.; Zhang, Y.B.; Grant, M.L.; Wilde, S.A.; Jahn, B.M. Geochronology of the Phanerozoic granitoids in northeastern China. *J. Asian Earth Sci.* **2011**, *41*, 1–30. [CrossRef]
29. Xu, W.L.; Wang, F.; Pei, F.P.; Meng, E.; Tang, J.; Xu, M.J.; Wang, W. Mesozoic tectonic regimes and regional ore-forming background in NE China: Constraints from spatial and temporal variations of Mesozoic volcanic rock associations. *Acta Petrol. Sin.* **2013**, *29*, 339–353. (In Chinese with English Abstract)
30. Liu, Y.J.; Zhang, X.Z.; Jin, W.; Chi, X.G.; Wang, C.W.; Ma, Z.H.; Han, G.Q.; Wen, Q.B.; Li, W.; Wang, W.D.; et al. Late Paleozoic tectonic evolution in Northeast China. *Geol. China* **2010**, *37*, 943–951, (In Chinese with English Abstract)
31. Zhou, J.B.; Wilde, S.A.; Zhang, X.Z.; Zhao, G.C.; Liu, F.L.; Qiao, D.W.; Ren, S.M.; Liu, J.H. A N1300 km late Pan-African metamorphic belt in NE China: New evidence from the Xing'an block and its tectonic implications. *Tectonophysics* **2011**, *509*, 280–292. [CrossRef]

32. Zhou, J.B.; Wilde, S.A.; Zhang, X.Z.; Ren, S.M.; Zheng, C.Q. Early Paleozoic metamorphic rocks of the Erguna block in the Great Xing'an Range, NE China: Evidence for the timing of magmatic and metamorphic events and their tectonic implications. *Tectonophysics* **2011**, *499*, 105–117. [CrossRef]
33. Zhou, J.B.; Wang, B.; Wilde, S.i.m.o.n.A.; Zhao, G.C.; Cao, J.L.; Zheng, C.Q.; Zeng, W.S. Geochemistr-y and U-Pb zircon dating of the Toudaoqiao blueschists in the Great Xing'an Range, Northeast China, and tectonic implications. *J. Earth Sci.* **2015**, *97*, 197–210.
34. Zhou, J.B.; Wilde, S.A. The crustal accretion history and tectonic evolution of the NE China segment of the Central Asian Orogenic Belt. *Gondwana Res.* **2013**, *23*, 1365–1377. [CrossRef]
35. Han, G.Q.; Liu, Y.J.; Neubauer, F.; Genser, J.; Li, W.; Zhao, Y.L.; Liang, C.Y. Origin of terranes in the eastern Central Asian Orogenic Belt, NE China: U-Pb ages of detrital zircons from Ordovician-Devonian sandstones, North Great Xing'an Range. *Tectonophysics* **2011**, *511*, 109–124. [CrossRef]
36. Han, G.Q.; Liu, Y.J.; Neubauer, F.; Genser, J.; Zhao, Y.L.; Wen, Q.B.; Li, W.; Wu, L.N.; Jiang, X.Y.; Zhao, L.M. Provenance analysis of Permian sandstones in the central and southern Da Xing'an Mountains, China: Constraints on the evolution of the eastern segment of the Central Asian Orogenic Belt. *Tectonophysics* **2012**, *580*, 100–113. [CrossRef]
37. Han, G.Q.; Liu, Y.J.; Neubauer, F.; Jin, W.; Genser, J.; Ren, S.M.; Li, W.; Wen, Q.B.; Zhao, Y.L.; Liang, C.Y. LA-ICP-MS U-Pb dating and Hf isotopic compositions of detrital zircons from the Permian sandstones in Da Xing'an Mountains, NE China: New evidence for the eastern extension of the Erenhot-Hegenshan suture zone. *J. Asian Earth Sci.* **2012**, *49*, 249–271. [CrossRef]
38. Han, G.Q.; Liu, Y.J.; Neubauer, F.; Bartel, E.; Genser, J.; Feng, Z.Q.; Zhang, L.; Yang, M.C. U-Pb age and Hf isotopic data of detrital zircons from the Devonian and Carboniferous sandstones in Yimin area, NE China: New evidences to the collision timing between the Xing'an and Erguna blocks in eastern segment of Central Asian Orogenic Belt. *J. Asian Earth Sci.* **2015**, *97*, 211–228. [CrossRef]
39. Xu, B.; Zhao, P.; Bao, Q.Z.; Zhou, Y.H.; Wang, Y.Y.; Luo, Z.W. Preliminary study on the pre-Mesozoic tectonic unit division of the Xing-Meng Orogenic Belt (XMOB). *Acta Petrol. Sin.* **2014**, *30*, 1841–1857. (In Chinese with English Abstract)
40. Xu, B.; Zhao, P.; Wang, Y.Y.; Liao, W.; Luo, Z.W.; Bao, Q.Z.; Zhou, Y.H. The pre-Devonian tectonic framework of Xing'an-Mongolia Orogenic belt (XMOB) in north China. *J. Asian Earth Sci.* **2015**, *97*, 183–196. [CrossRef]
41. Ma, Y.F.; Liu, Y.J.; Peskov, A.Y.; Wang, Y.; Song, W.M.; Zhang, Y.J.; Qian, C.; Liu, T.J. Paleozoic tectonic evolution of the eastern Central Asian Orogenic Belt in NE China. *China Geol.* **2022**, *5*, 555–578. [CrossRef]
42. Li, J.Y.; Liu, J.F.; Qu, J.F.; Zheng, R.G.; Zhao, S.; Zhang, J.; Wang, L.J.; Zhang, X.W. Paleozoic tectonic units of Northeast China: Continental Blocks or Orogenic Belts? *Earth Sci.* **2019**, *44*, 3157–3177. (In Chinese with English Abstract)
43. Li, R.S. Xinlin Ophiolite. *Heilongjiang Geol.* **1991**, *2*, 19–32. (In Chinese with English Abstract)
44. Ye, H.W.; Zhang, X.Z.; Zhou, Y.W. The texture and evolution of Manzhouli—Suifenhe lithosphere-study based on features of blueschist and ophiolites. In *Geological Studies of Lithospheric Structure andEvolution of Manzhouli-Suifenhe Geotransect, China*; MSGT Geology Group, Ed.; Seismological Press: Beijing, China, 1994; pp. 73–83. (In Chinese with English Abstract)
45. Hu, D.G.; Tan, C.X.; Zhang, H. Middle Proterozoic Ophiolites in the Alihe area. Inner Mongolia. *Reg. Geol. China* **1995**, *4*, 334–339. (In Chinese with English Abstract)
46. Hu, D.G.; Zheng, Q.D.; Fu, J.Y.; Liu, X.G. The geological and geochemical characteristics of the Jifeng Komatiites in the Da Hinggan Ling Mountains. *J. Geomech.* **2001**, *7*, 111–115. (In Chinese with English Abstract)
47. Hu, D.G.; Li, H.W.; Liu, X.G.; Yu, R.W. Dating of Sm-Nd isochron Ages of the Jifeng Komatiites from the Da Xing'an Ling. *Acta Geosci. Sin.* **2003**, *24*, 405–408. (In Chinese with English Abstract)
48. Zhu, K.Y.; Yang, J.X. The remains and history of evolution of the plate tectonics in the Geosynclinal region in the northern part of Inner Mongolia. *Reg. Geol. China* **1991**, *4*, 335–341. (In Chinese with English Abstract)
49. Zhong, H.; Fu, J.Y. Petrochemistry, geochemistry and genesis of the metagabbro in Tayuan, Northern Daxing'anling. *Geol. Resour.* **2006**, *15*, 42–47. (In Chinese with English Abstract)
50. Feng, Z.Q.; Liu, Y.J.; Liu, B.Q.; Wen, B.Q.; Li, W.M.; Liu, Q. Timing and nature of the Xinlin–Xiguitu Ocean: Constraints from ophiolitic gabbros in the northern Great Xing'an Range, eastern Central Asian Orogenic Belt. *Int. J. Earth Sci.* **2016**, *105*, 491–505. [CrossRef]
51. Du, B.Y.; Feng, Z.Q.; Liu, Y.W.; Zhang, T.A.; Zhao, M.S.; Zhao, Y.S.; Zhen, M. Determination of Neoproterozoic meta-gabbro from Huanerku, Da Hinggan Mountains and its geological significance. *Glob. Geol.* **2017**, *36*, 751–762. (In Chinese with English Abstract)
52. She, H.Q.; Li, J.W.; Xiang, A.P.; Guan, J.D.; Zhang, D.Q.; Yang, Y.C.; Tan, G.; Zhang, B. U–Pb ages of the zircons from primary rocks in the middle–northern Daxinganling and its implications to geotectonic evolution. *Acta Petrol. Sin.* **2012**, *28*, 571–594. (In Chinese with English Abstract)
53. Shi, Z.W.; Bai, Z.D.; Dong, G.C.; Santosh, M.; Li, L.Y.; Luo, Z.B.; Liu, T.; Wang, K.Q. Supra-subduction zone ophiolite from the Great Xing'an Range, China: Geochemistry, geochronology, and implication for formation in a back-arc setting. *Geol. J.* **2021**, *57*, 1783–1802. [CrossRef]
54. Wu, G.; Chen, Y.C.; Sun, F.Y.; Liu, J.; Wang, G.R.; Xu, B. Geochronology, geochemistry, and Sr–Nd–Hf isotopes of the early Paleozoic igneous rocks in the Duobaoshan area, NE China, and their geological significance. *J. Asian Earth Sci.* **2015**, *97*, 229–250. [CrossRef]
55. Zhao, C.; Qin, K.Z.; Song, G.X.; Li, G.M.; Li, Z.Z. Early Palaeozoic high-Mg basalt-andesite suite in the Duobaoshan Porphyry Cu deposit, NE China: Constraints on petrogenesis, mineralization, and tectonic setting. *Gondwana Res.* **2019**, *71*, 91–116. [CrossRef]

56. Chen, A.X.; Zhou, D.; Zhang, Q.K.; Guan, P.Y.; Yang, B. Tectonic and sedimentary environment in the Ordovician period of Central Xing'an Block. *Geoscience* **2016**, *30*, 1061–1071. (In Chinese with English Abstract)
57. Li, L.Y.; Liu, B. Sedimentary geological characteristics and sediment source of Luohe Formation in Wunuer Area, Great Xing'an Range. *Mod. Min.* **2020**, *617*, 37–45. (In Chinese with English Abstract)
58. Zhang, H.H.; Xu, D.B.; Zhang, K. Geochemical characteristic and sedimentary environment of the Devonian Niqiuhe Formation in northern Daxinganling Range. *Geol. Resour.* **2014**, *23*, 316–322. (In Chinese with English Abstract)
59. Zhang, Y.J.; Zhang, C.; Wu, X.W.; Cui, T.R.; Yang, Y.J.; Chen, H.J.; Jiang, B.; Guo, W.; Ma, Y.F. Geochronology and geochemistry of Late Paleozoic marine volcanic from the Zhalantun Area in Northern DaHinggan Mountains and its geological significance. *Acta Geol. Sin.* **2016**, *90*, 2706–2720. (In Chinese with English Abstract)
60. Zhao, Z.; Chi, X.G.; Pan, S.Y.; Liu, J.F.; Sun, W.; Hu, Z.C. Zircon U-Pb LA-ICP-MS dating of Carboniferous volcanics and its geological significance in the northwestern Lasser Xing'an Range. *Acta Petrol. Sin.* **2010a**, *26*, 2452–2464. (In Chinese with English Abstract)
61. Li, L.Y.; Chen, M.; Gong, Q.D.; Zhang, C.H.; Wang, X. Zircon U-Pb age, geochemical characteristics and geological significance of syenogranite in Wunuer area, Great Hinggan Mountains. *Geol. Rev.* **2019**, *65*, 389–400. (In Chinese with English Abstract)
62. Ludwig, K.R. *2003.ISOPLOT 3.00: A Geochronological Toolkit for Microsoft Excel*; Berkeley Geochronology Center: Berkeley, CA, USA.
63. Middlemost, E.A.K. Naming materials in the magma/igneous rock system. *Earth-Sci. Rev.* **1994**, *37*, 215–224. [CrossRef]
64. Maniar, P.D.; Piccoli, P.M. Tectonic discrimination of granitoids. *Geol. Soc. Am. Bull.* **1989**, *101*, 635–643. [CrossRef]
65. Rickwood, P.C. Boundary lines within petrologic diagrams which use oxides of major and minor elements. *Lithos* **1989**, *22*, 247–263. [CrossRef]
66. Zhao, Z.; Chi, X.G.; Liu, J.F.; Wang, T.F.; Hu, Z.C. Late Paleozoic arc-related magmatism in Yakeshi region, Inner Mongolia Chronological and geochemical evidence. *Acta Petrol. Sin.* **2010b**, *26*, 3245–3258. (In Chinese with English Abstract)
67. Zhang, Y.; Pei, F.P.; Wang, Z.W.; Xu, W.L.; Li, Y.; Wang, F.; Zhou, Z.B. Late Paleozoic tectonic evolution of the central Great Xing'an Range, northeast China: Geochronological and geochemistry evidence from igneous rocks. *Geol. J.* **2018**, *53*, 282–303. [CrossRef]
68. Jia, X.; Ren, J.G.; Xu, W.T.; Ma, H.C.; Zhang, C.; Shi, G.M. Zircon U-Pb dating of Late Paleozoic alkali-feldspar granite in Duobaoshan, Great Xing'an Range: Constrains on collision time of Xiang'an and Songnen Blocks. *Geol. China* **2022**, *49*, 586–600. (In Chinese with English Abstract)
69. Shi, L.; Zheng, C.Q.; Yao, W.G.; Li, J.; Cui, F.H.; Cao, F.; Han, X.M. Geochronological framework and tectonic setting of the granitic magmatism in the Chaihe-Moguqi region, central Great Xing'an Range, China. J. *Asian Earth Sci.* **2015**, 443–453. [CrossRef]
70. Ma, Y.F.; Liu, Y.J.; Qin, T.; Sun, W.; Zang, Y.Q. Carboniferous granites in the Jalaid Banner area, middle Great Xing'an Range, NE China: Petrogenesis, tectonic background and orogeny accretionary implications. *Acta Petrol. Sin.* **2018**, *34*, 2931–2955. (In Chinese with English Abstract)
71. Ma, Y.F.; Liu, Y.J.; Qin, T.; Sun, W.; Zang, Y.Q.; Zhang, Y.J. Late Devonian to early Carboniferous magmatism in the western Songliao–Xilinhot block, NE China: Implications for eastward subduction of the Nenjiang oceanic lithosphere. *Geol. J.* **2020**, *55*, 2208–2231. [CrossRef]
72. Ma, Y.F.; Liu, Y.J.; Wang, Y.; Qin, T.; Chen, H.J.; Sun, W.; Zang, Y.Q. Late Carboniferous mafic to felsic intrusive rocks in the central Great Xing'an Range, NE China: Petrogenesis and tectonic implications. *Int. J. Earth Sci.* **2020**, *109*, 761–783. [CrossRef]
73. Feng, Z.Q.; Li, W.M.; Liu, Y.J.; Jin, W.; Wen, Q.B.; Liu, B.Q.; Zhou, J.P.; Zhang, T.A.; Li, X.Y. Early Carboniferous tectonic evolution of the northern Heihe–Nenjiang–Hegenshan suture zone, NE China: Constraints from the mylonitized Nenjiang rhyolites and the Moguqi gabbros. *Geol. J.* **2018**, *53*, 1005–1021. [CrossRef]
74. Abdel-Karim, A.-A.M.; Azer, M.K.; Mogahed, M.M. Neoproterozoic concentric intrusive complex of gabbro-diorite-tonalite-granodiorite association, Rahaba area, southern Eastern Desert of Egypt: Implications for magma mixing of arc intrusive rocks. *Lithos* **2021**, *404–405*, 106423. [CrossRef]
75. Altherr, R.; Siebel, W. I-type plutonism in a continental back-arc setting: Miocene granitoids and monzonites from the Central Aegean Sea, Greece. *Contrib. Miner. Pet.* **2002**, *143*, 397–415. [CrossRef]
76. Clemens, J.D.; Stevens, G.; Farina, F. The enigmatic sources of I-type granites: The peritectic connexion. *Lithos* **2011**, *126*, 174–181. [CrossRef]
77. Mogahed, M.M.; Abdelfadil, K.M. Constraints of Mantle and Crustal Sources Interaction during Orogenesis of Pre-and Post-collision Granitoids from the Northern Arabian-Nubian Shield: A Case Study from Wadi El-Akhder Granitoids, Southern Sinai, Egypt. *Acta Geol. Sin.-Engl. Ed.* **2021**, *95*, 1527–1550. [CrossRef]
78. Yu, Y.; Sun, M.; Long, X.; Li, P.; Zhao, G.; Kröner, A.; Broussolle, A.; Yang, J. Whole-rock Nd–Hf isotopic study of I-type and peraluminous granitic rocks from the Chinese Altai: Constraints on the nature of the lower crust and tectonic setting. *Gondwana Res.* **2017**, *47*, 131–141. [CrossRef]
79. Zhao, X.F.; Zhou, M.F.; Li, J.W.; Wu, F.Y. Association of Neoproterozoic A-and I-type granites in South China: Implications for generation of A-type granites in a subduction-related environment. *Chem. Geol.* **2008**, *257*, 1–15. [CrossRef]
80. Sun, S.S.; McDonough, W.F. Chemical and isotopic systematics of ocean basalts: Implications for mantle composition and processes. In *Magmatism in Ocean Basins*; Saunders, A.D., Norry, M.J., Eds.; Geological Society Special Publication: London, UK, 1989; Volume 42, pp. 313–345.
81. Whalen, J.B.; Currie, K.L.; Chappell, B.W. A-Type granites: Geochemical characteristics, discrimination and petrogenesis. *Contrib. Mineral. Petrol.* **1987**, *95*, 407–419. [CrossRef]

82. Chappell, B.; White, A.J.R. I- and S-type granites in the Lachlan Fold Belt. *Trans. R. Soc. Edinb. Earth Sci.* **1992**, *83*, 1–26.
83. Pearce, J.A.; Harris, N.B.W.; Tindle, A.G. Trace element discrimination diagrams for the tectonic interpretation of granitic rocks. *J. Petrol.* **1984**, *25*, 956–983. [CrossRef]
84. Harris, R.A.; Stone, D.B.; Turner, D.L. Tectonic implications of paleomagnetic and geochronologic data from the Yukon-Koyukuk province, Alaska. *Geol. Soc. Am. Bull.* **1987**, *99*, 362–375. [CrossRef]
85. Grove, T.L.; Elkins-Tanton, L.T.; Parman, S.W.; Cartterjee, N.; Muntener, O.; Gaetani, G.A. Fractional crystallization and mantle melting controls on calk-alkaline differentiation trends. *Contrib. Mineral. Petrol.* **2003**, *145*, 515–533. [CrossRef]
86. Tang, J.; Xu, W.L.; Wang, F.; Wang, W.; Xu, M.J.; Zhang, Y.H. Geochronology and geochemistry of Neoproterozoic magmatism in the Erguna Massif, NE China: Petrogenesis and implications for the breakup of the Rodinia supercontinent. *Precambrian Res.* **2013**, *224*, 597–611. [CrossRef]
87. Tang, J.; Xu, W.L.; Wang, F.; Wang, W.; Xu, M.J.; Zhang, Y.H. Geochronology and geochemistry of Early-Middle Triassic magmatism in the Erguna Massif, NE China: Constraints on the tectonic evolution of the Mongol-Okhotsk Ocean. *Lithos* **2014**, *184–187*, 1–16. [CrossRef]
88. Li, Y.; Xu, W.L.; Wang, F.; Tang, J.; Pei, F.P.; Wang, Z.J. Geochronology and geochemistry of late Paleozoic volcanic rocks on the western margin of the Songnen-Zhangguangcai Range Massif, NE China: Implications for the amalgamation history of the Xing'an and Songnen-Zhangguangcai Range massifs. *Lithos* **2014**, *205*, 394–410. [CrossRef]
89. Zhu, X.Y.; Liu, G.P. Geochemical characteristics of Paleozoic margine volcanic rocks in Southern Hulun Buir League, Inner Mongolia, and their geological significance. *Acta Petrol. Et Mineral.* **1995**, *14*, 109–118. (In Chinese with English Abstract)
90. Li, J.Y. Some new ideas on tectonics of NE China and its neighboring areas. *Geol. Rev.* **1998**, *44*, 339–347. (In Chinese with English Abstract)
91. Stern, R.J. Subduction zones. *Rev. Geophys.* **2002**, *40*, 3-1–3-38. [CrossRef]
92. Li, J.Y.; Zhang, J.; Yang, T.N.; Li, Y.P.; Sun, G.H.; Zhu, Z.X.; Wang, L.J. Crustal tectonic vivision and evolution of the southern part of the North Asian Orogenic Region and its adajacent Areas. *J. Jilin Univ. (Earth Sci. Ed.)* **2009**, *39*, 584–605. (In Chinese with English Abstract)
93. Zhang, Y.L.; Ge, W.C.; Gao, Y.; Chen, J.S.; Zhao, L. Zircon U-Pb ages and Hf isotopes of granites in Longzhen area and their geological implication. *Acta Petrol. Sin.* **2010**, *26*, 1059–1073. (In Chinese with English Abstract) [CrossRef]
94. Ren, X.H.; He, Z.H.; Wang, Q.H.; Zhou, X.M.; Zhao, D.; He, Y.; Ge, W.C. Pertogenesis of Late Paleozoic granites from Yaergenchu area in north-central Great Xing'an Range and its geological implication. *Glob. Geol.* **2017**, *36*, 41–53. (In Chinese with English Abstract)
95. Zhou, C.Y.; Wu, F.Y.; Ge, W.C.; Sun, D.Y.; Abdel, R.A.; Zhang, J.H.; Cheng, R.Y. Age, geochemistry and petrogenesis of the cumulate gabbro in Tahe, northern Da Hinggan Mountain. *Acta Petrol. Sin.* **2005**, *21*, 763–775. (In Chinese with English Abstract)
96. Zhao, Q. The Genetic Type and Geological Significe of Late Paleozoic Granites in Yakeshi Region, North Great Xing'an Range. China. Master's thesis, University of Geosciences, Beijing, China, 2012; pp. 1–83. (In Chinese with English Abstract)
97. Sun, D.Y.; Wu, F.Y.; Li, H.M.; Lin, Q. Emplacement age of the post-orogenic A-type granites in Northwestern Lesser Xing'an Range, and its relationship to the eastward extension of Suolushan-Hegenshan-Zhalaite collisional suture zone. *Chin. Sci. Bull.* **2000**, *45*, 2217–2222. (In Chinese with English Abstract)